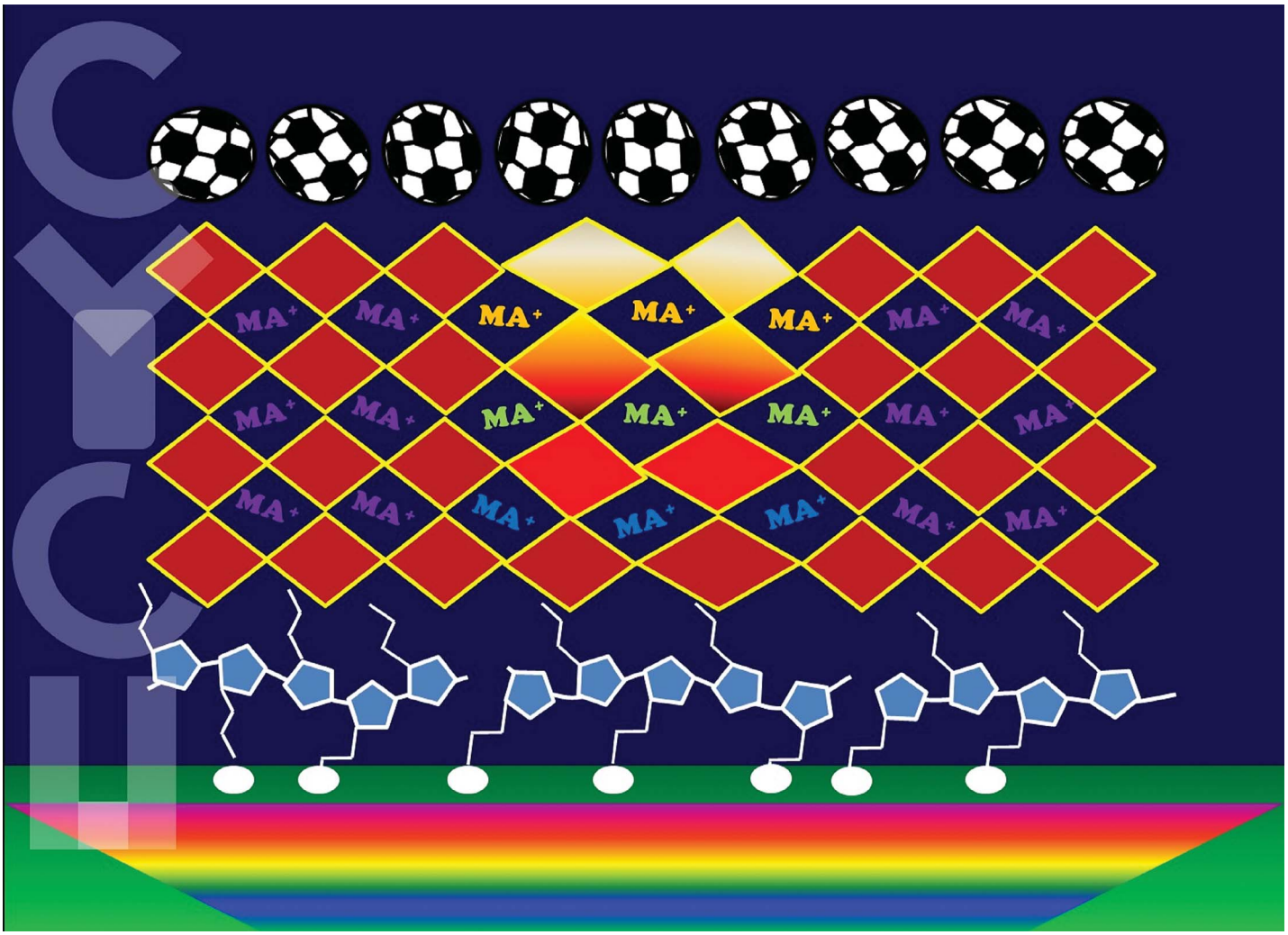

Showcasing research from Professor Sheng Hsiung Chang's laboratory, Department of Physics, Chung Yuan Christian University, Taiwan, Republic of China.

Effects of drying time on the formation of merged and soft $MAPbI_3$ grains and their photovoltaic responses

A suitable drying time of the perovskite precursor solution can facilitate the formation of merged grains while maintaining the interfacial contact quality between the perovskite thin film and hole transport layer, which highly increases the open-circuit voltage (V_{OC}) from 1.01 V to 1.15 V after 30 days and thereby improving the device performance and lifespan of the resultant inverted perovskite photovoltaic cells. It is noted that the V_{OC} of the photovoltaic cells is still higher than 1.15 V after 80 days.

As featured in:

See Hsin-Ming Cheng, Sheng Hsiung Chang *et al.*, *Nanoscale Adv.*, 2023, **5**, 2190.

ROYAL SOCIETY OF CHEMISTRY

rsc.li/nanoscale-advances

Registered charity number: 207890

Nanoscale Advances

ROYAL SOCIETY OF CHEMISTRY

PAPER

View Article Online
View Journal | View Issue

Cite this: *Nanoscale Adv.*, 2023, **5**, 2190

Effects of drying time on the formation of merged and soft $MAPbI_3$ grains and their photovoltaic responses†

Anjali Chandel,[abc] Qi Bin Ke,[abc] Shou-En Chiang,[abc] Hsin-Ming Cheng *[d] and Sheng Hsiung Chang *[abc]

The grain sizes of soft $CH_3NH_3PbI_3$ ($MAPbI_3$) thin films and the atomic contact strength at the $MAPbI_3$/P3CT-Na interface are manipulated by varying the drying time of the saturated $MAPbI_3$ precursor solutions, which influences the device performance and lifespan of the resultant inverted perovskite photovoltaic cells. The atomic-force microscopy images, cross-sectional scanning electron microscopy images, photoluminescence spectra and absorbance spectra show that the increased short-circuit current density (J_{SC}) and increased fill factor (FF) are mainly due to the formation of merged $MAPbI_3$ grains. Besides, the open-circuit voltage (V_{OC}) of the encapsulated photovoltaic cells largely increases from 1.01 V to 1.15 V, thereby increasing the power conversion efficiency from 17.89% to 19.55% after 30 days, which can be explained as due to the increased carrier density of the $MAPbI_3$ crystalline thin film. It is noted that the use of the optimized drying time during the spin coating process results in the formation of merged $MAPbI_3$ grains while keeping the contact quality at the $MAPbI_3$/P3CT-Na interface, which boosts the device performance and lifespan of the resultant perovskite photovoltaic cells.

Received 19th December 2022
Accepted 2nd March 2023

DOI: 10.1039/d2na00929c

rsc.li/nanoscale-advances

Introduction

Solution-processed perovskite crystalline thin films have been widely used in various applications, such as photovoltaic cells,[1–3] light-emitting diodes,[4–6] photo-detectors,[7–9] memory devices[10–12] and field-effect transistors,[13–15] mainly due to their tunable crystal structure and superior optoelectronic properties.[16–18] Organometal trihalide perovskites are suitable for solar cells as the light absorbing layer owing to the large absorption coefficient, moderate refractive index, small exciton binding energy and long carrier diffusion length,[19–21] which results in a high power conversion efficiency (PCE) of 25.6% (25.0%) when the regular-type (inverted-type) structure is used.[22,23] In the lead trihalide perovskite photovoltaic cells, the size of the multi-crystalline grains was increased from several hundred nanometers to several micrometers in order to reduce the defect density at the grain boundaries of the light absorbing layer.[24–26] However, the larger grain (lower surface area) corresponds to the lower doping concentration of the perovskite crystalline thin film, thereby resulting in the lower open-circuit voltage (V_{OC}) of the resultant cells.[27–29] In other words, the ideal V_{OC} of the intrinsic perovskite based photovoltaic cells is related to the Fermi levels of the electron transport layer (ETL) and hole transport layer (HTL).[30–32] In recent years, the power conversion efficiency (PCE) of the perovskite photovoltaic cells can be higher than 20% when the grains of the light absorbing layer are sub-micrometer size,[33–35] which means that the defects at the grain boundaries are effectively passivated, thereby resulting in low carrier recombination (high fill factor). In other words, there is an optimal grain size of the perovskite crystalline thin films in the highly efficient and stable perovskite photovoltaic cells. In the highly efficient and stable perovskite photovoltaic cells, the grain sizes of the light absorbing layer are ranging from 300 nm to 500 nm,[22,23,33–35] which is slightly larger than the size of the surface feature in the ITO thin film.[36,37] It is noted that the layered structure is a common feature of these perovskite grains,[38] which indicates that the sub-micrometer-sized particles are single-crystalline grains.[39] In other words, the optimized size of perovskite grains is highly related to the size of the surface feature in the ITO thin film. On the other hand, the residual solvent molecules in the solution-processed perovskite grain thin films degrade the device performance and lifespan of the resultant photovoltaic cells,[40–42] which indicates the importance of the drying process during the formation of high-quality perovskite thin films.

[a]*Department of Physics, Chung Yuan Christian University, Taoyuan 320314, Taiwan, Republic of China. E-mail: shchang@cycu.edu.tw*

[b]*Research Center for Semiconductor Materials and Advanced Optics, Taoyuan 320314, Taiwan, Republic of China*

[c]*Center for Nano Technology and R&D Center for Membrane Technology, Chung Yuan Christian University, Taoyuan 320314, Taiwan, Republic of China*

[d]*Department of Photonics, National Cheng Kung University, Tainan 701, Taiwan, Republic of China. E-mail: smcheng.jemmy@gmail.com*

† Electronic supplementary information (ESI) available. See DOI: https://doi.org/10.1039/d2na00929c

In this study, the main aim is to investigate the effects of the perovskite grain size on the device performance of the P3CT-Na HTL based inverted perovskite photovoltaic cells with a facile encapsulation method.[43] Our experimental results show that the re-dissolving process of perovskite nucleation can be used to manipulate the grain size of the perovskite crystalline thin films which strongly influences the V_{OC} and lifespan of the encapsulated perovskite photovoltaic cells.

Experiments

Poly[3-(4-carboxybutyl)thiophene-2,5-diyl] (P3CT) and NaOH were purchased from Matrix Scientific and Sigma-Aldrich, respectively. The regioregularity of the used P3CT polymers is about 85%. PbI_2 and CH_3NH_3I (MAI) were purchased from Uni-Onward and Lumtec, respectively. Phenyl-C_{61}-butyric acid methyl ester (PCBM) and (bathocuproine) BCP were purchased from Uni-Onward and Sigma-Aldrich, respectively. Dimethylformamide (DMF), dimethyl sulfoxide (DMSO), chlorobenzene (CB) and bromobenzene (BrB) were purchased from Sigma-Aldrich. Isopropyl alcohol (IPA) was purchased from ACROS. The preparation of P3CT-Na/water solution, $MAPbI_3$/DMF:DMSO solution, PCBM/CB:BrB solution and BCP/IPA solution is illustrated in our previous report.[44] The P3CT-Na solution, perovskite precursor (1.5 M) solution, PCBM/CB:BrB solution (2 wt%) and BCP/IPA (0.089 wt%) solution were stirred at 500 rpm for 3 h at room temperature.

The device structure is Ag/BCP:PCBM/$MAPbI_3$/P3CT-Na/ITO/glass. Ag and ITO are used as the cathode and anode, respectively. PCBM and P3CT-Na are used as the electron transport layer (ETL) and hole transport layer (HTL), respectively. BCP is used to modify the PCBM thin film and the contact quality at the PCBM/$MAPbI_3$ interface.[45] A $MAPbI_3$ crystalline thin film is used as the light absorbing layer. The ITO/glass (7 Ω sq^{-1}) substrates were modified by using a UV–ozone cleaner for 45 minutes in order to increase the surface wettability. The P3CT-Na polymer modification layer, 500 nm-thick $MAPbI_3$ crystalline thin film, and 60 nm-thick PCBM thin film were fabricated by using the spin coating method. Besides, the BCP/IPA solution treatment was used to modify the PCBM thin film and the contact quality at the PCBM/$MAPbI_3$ interface. The 100 nm-thick Ag thin film was fabricated by using the vacuum thermal evaporation method. The detailed information of the device fabrication process is illustrated in our previous report.[44] The fabrication conditions of the P3CT-Na polymer ultra-thin layer, $MAPbI_3$ crystalline thin film, PCBM thin film and Ag thin film are described in the ESI.† After the injection of CB into the $MAPbI_3$ precursor solution, the precursor turns from a transparent solution to a light brown solution, thereby forming nucleation sites and/or intermediate states. In other words, the residual spin period can be viewed as the drying time of the $MAPbI_3$ precursor solution. During the spin coating process of the $MAPbI_3$ precursor solution, the spin time in the second step was changed from 29 s to 49 s in order to vary the drying times from 20 s to 40 s. The active area of a single $MAPbI_3$ photovoltaic device is defined to be 2 $\times$ 5 mm^2 by using a metallic shadow mask during the thermal evaporation process of Ag thin films. Each sample contains four cells. One glass substrate and one Parafilm were used to encapsulate the device in order to increase the device lifespan. The encapsulation method is described in Fig. S1.† The current density–voltage (J–V) curves of the inverted perovskite photovoltaic cells were obtained by using a source-meter system (NI-USB 6356 DAQ) under one sun illumination (AM1.5G, 100 mW cm^{-2}). The light intensity of the light-emitting diode based solar simulator (VeraSol-2, Newport) was calibrated by using a reference cell (91150V, Newport) before the J–V curve measurement.

To investigate the trends of the V_{OC}, J_{SC} and FF, $MAPbI_3$/P3CT-Na/ITO/glass samples with and without encapsulation were prepared. An atomic force microscope (UTEK, Nanoview 1000) and field-emission scanning electron microscope (JEOL, JSM-7600F) were used to obtain the surface morphologies and cross-sectional images of the samples, respectively. An X-ray diffractometer (Bruker, D8 Advance) was used to characterize the crystal structures of the samples. A home-made optical spectrometer was used to measure the absorbance and reflectance spectra. The setup of the absorbance/reflectance spectrometer is illustrated in Fig. S2.† A home-made optical microscope based photoluminescence (PL) spectrometer[46] was used to analyze the light emissions of the samples under top excitation and bottom excitation.

Results and discussion

Fig. 1 presents the J–V curves of the inverted perovskite photovoltaic cells under one sun illumination (AM 1.5G, 100 mW cm^{-2}). The photovoltaic performance of the 8 cells for each condition is listed in Table 1. The average V_{OC} increases from 1.010 V to 1.017 V with the increase in the drying time from 20 s to 40 s, which means that a longer drying time results in a lower potential loss. When the drying time increases from 20 s (30 s) to 30 s (40 s), the average J_{SC} increases (decreases) from 19.01 mA cm^{-2} (22.25 mA cm^{-2}) to 22.25 mA cm^{-2} (20.32 mA cm^{-2}), which means that the drying time largely influences the contact quality at the $MAPbI_3$/P3CT-Na interface, thereby dominating the collection efficiency of photo-generated holes.[47] The photovoltaic cells were encapsulated with a facile method on the 2nd day in order to increase the device lifespan.[43] It is noted that the V_{OC} values increased after the encapsulation process. When the drying time is 20 s, the J_{SC} and FF are both increased after the encapsulation process. When the drying time is 30 s or 40 s, the J_{SC} and FF are both decreased after the encapsulation process, thereby slightly decreasing the PCE on the 2nd day. Besides, the V_{OC} hysteresis of the encapsulated solar cells largely increases from 0.033 V to 0.220 V with the increase in the drying time from 30 s to 40 s (see Fig. S3†), which can be used to explain the lower V_{OC} and FF when the drying time is 40 s. On the 80th day, the V_{OC} and J_{SC} values are both increased while maintaining the high FF values. The slightly decreased FF is mainly due to the increased series resistance (R_S). Fig. 2 presents the J–V curves of the inverted perovskite photovoltaic cells on the 2nd day and 80th day. The V_{OC} and J_{SC} values of the encapsulated photovoltaic cells are both increased, which means that the encapsulation process increases (reduces) the

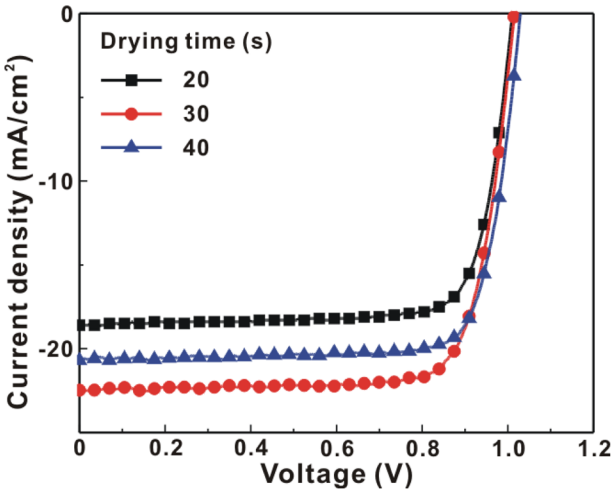

Fig. 1 Current density–voltage (J–V) curves of the photovoltaic cells under one sun illumination (AM 1.5G, 100 mW cm^{-2}). $MAPbI_3$ perovskite films are prepared with different drying times.

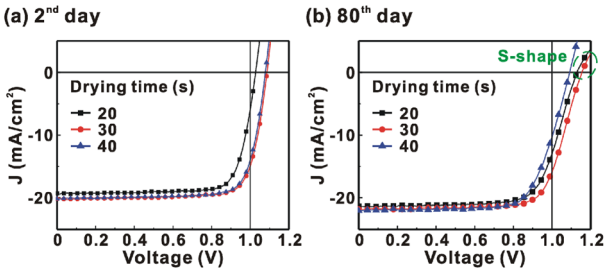

Fig. 2 Current density–voltage (J–V) curves of the photovoltaic cells with a facile encapsulation method under one sun illumination (AM 1.5G and 100 mW cm^{-2}). $MAPbI_3$ perovskite films are prepared with different drying times. (a) 2nd day; (b) 80th day.

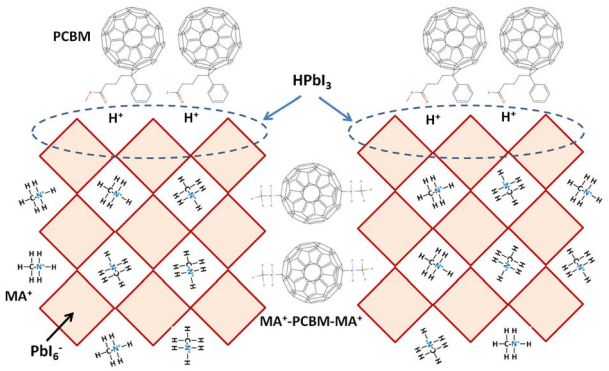

Fig. 3 Formation of MA^+-PCBM-MA^+ cations and an $HPbI_3$ interlayer.

exciton dissociation efficiency (potential loss). When the drying time is 20 s or 30 s, an s-shape characteristic can be observed in the J–V curves, which means that an ultra-thin potential barrier may be formed at the PCBM/$MAPbI_3$ interface.[48] In other words, it is possible to form a large-bandgap $HPbI_3$ interlayer[49] in between the PCBM and $MAPbI_3$ thin films due to the formation of MA^+-PCBM-MA^+ cations,[50] as shown in Fig. 3. The formation of a MA^+-PCBM-MA^+ cation produces two H^+ ions *via* dehydrogenation from the two MA^+ cations. Then, it is possible to form a $HPbI_3$ interlayer when the H^+ ions migrate to MA^+ vacancies. It is noted that the s-shape characteristics are not observed in the J–V curves when the drying time is 40 s. Fig. 4 presents the day-dependent device performance of the best perovskite photovoltaic cells under one sun illumination. After encapsulation, the photovoltaic cells have similar trends in the day-dependent V_{OC}, J_{SC} and FF. When the drying time is 30 s, the V_{OC} (FF) of the encapsulation photovoltaic cell largely increases (slightly decreases) from 1.087 V (78.1%) to 1.156 V (72.6%), thereby maintaining the average PCE to be higher than 17.5% within 80 days. On the 80th day, the higher average PCE of the encapsulated cells is mainly due to the higher average V_{OC} when the drying time is 30 s. And, the differences in average V_{OC} values are higher than the standard deviation values of V_{OC} (see Table 1), which can be used to confirm that the PCE and device lifespan of the resultant perovskite photovoltaic cells are better when the drying time is 30 s. To analyze the day-dependent device performance, the V_{OC} curves and FF curves are fitted with an exponential growth function and a linear decay function, respectively (see Fig. S4†). The rising time values of the V_{OC} curves (decay rates of the FF curves) are 11.59 days (−0.0015 per day), 19.83 days (−0.0008 per day) and 18.03 days (−0.0012 per day) when the drying times are 20, 30 and 40 s, respectively. The trend of the V_{OC} rising time values is inversely proportional to the trend of the FF decay rate values, which is probably related to the shallow defect density in the $MAPbI_3$ crystalline thin films

Table 1 Day-dependent device performance of photovoltaic cells under one sun illumination (AM 1.5G, and 100 mW cm^{-2})

Day/encapsulation	Drying time (s)	V_{OC} (V)	J_{SC} (mA cm^{-2})	FF (%)	PCE (%)	R_s (Ω)
1st/no	20	1.010 ± 0.001	19.01 ± 0.36	73.2 ± 5.3	14.05 ± 1.32	38 ± 1
1st/no	30	1.015 ± 0.001	22.25 ± 0.32	78.5 ± 0.4	17.72 ± 0.37	39 ± 1
1st/no	40	1.017 ± 0.001	20.32 ± 0.45	72.5 ± 6.5	14.98 ± 1.72	50 ± 5
2nd/with	20	1.043 ± 0.014	19.34 ± 0.04	75.1 ± 3.0	15.15 ± 0.85	58 ± 17
2nd/with	30	1.086 ± 0.001	20.00 ± 0.27	76.6 ± 1.5	16.63 ± 0.58	40 ± 1
2nd/with	40	1.045 ± 0.034	19.89 ± 0.31	70.1 ± 5.9	14.57 ± 1.99	48 ± 10
80th/with	20	1.109 ± 0.022	21.24 ± 0.17	72.8 ± 1.9	17.15 ± 0.94	98 ± 36
80th/with	30	1.133 ± 0.023	21.82 ± 0.05	71.9 ± 0.7	17.78 ± 0.57	112 ± 13
80th/with	40	1.092 ± 0.020	21.81 ± 0.26	68.5 ± 2.5	16.31 ± 1.11	152 ± 32

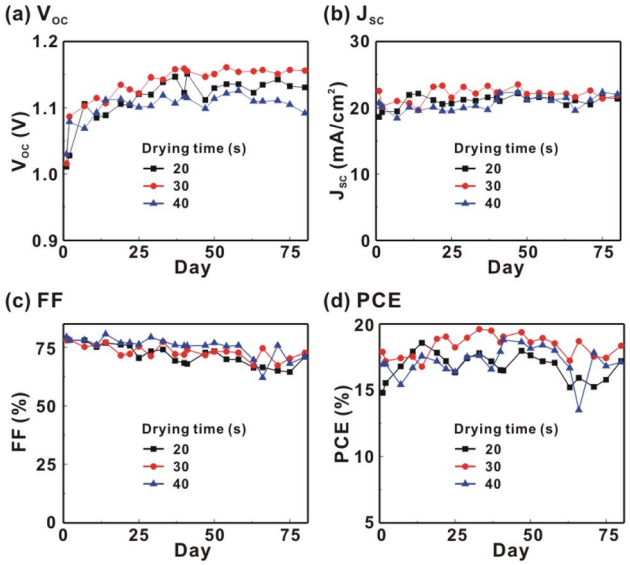

Fig. 4 Day-dependent device performance of the photovoltaic cells under one sun illumination (AM 1.5G and 100 mW cm^{-2}). $MAPbI_3$ perovskite films are prepared with different drying times. (a) V_{OC}; (b) J_{SC}; (c) FF; (d) PCE.

and the formation rate of MA^+-PCBM-MA^+ cations and a large-bandgap $HPbI_3$ interlayer at the PCBM/$MAPbI_3$ interface. The existence of shallow defects does not significantly influence the exciton binding energy of perovskite crystalline thin films.[43,51] In other words, the high V_{OC} of 1.156 V can be explained as due to the formation of shallow defects in the soft $MAPbI_3$ crystalline thin film.[52] To confirm the stable J_{SC} values, the incident photon-to-current conversion efficiency (IPCE) spectra of the encapsulated cells were measured on the 406th day, as shown in Fig. S5(a).† Fig. S5(b)† shows that the integrated current density values are about 22 mA cm^{-2} which is close to the stable J_{SC} values. It is noted that the highest PCE is lower than 20%, which is probably due to the lower regioregularity of the used P3CT polymers.[47]

Fig. 5 presents the atomic force microscopy (AFM) images and cross-sectional scanning electron microscopy (SEM) images of the $MAPbI_3$/P3CT-Na/ITO/glass samples fabricated with different drying times. When the drying time increases from 20 s to 40 s, the trend of the average surface roughness values (Fig. 5(a)–(c)) is proportional to the trend of the grain sizes (see Fig. 5(d)–(f)). In other words, the longer drying time results in merged $MAPbI_3$ grains, thereby increasing the surface roughness which can be calculated from the AFM images. It is noted that the $MAPbI_3$ crystalline thin film is separated from the substrate when the drying time is 30 s or 40 s, which means that the formation of merged $MAPbI_3$ grains reduces the atomic contact strength at the $MAPbI_3$/P3CT-Na interface, thereby leading to mechanical stress induced separation during the splitting process. In other words, there is a trade-off between the $MAPbI_3$ grain size and the contact quality at the $MAPbI_3$/P3CT-Na interface, which dominates the trends of the J_{SC} values and FF values of the resultant inverted perovskite photovoltaic cells on the first day (see Table 1). Besides, the trend of the grain sizes is proportional to the trend of the V_{OC} values and the s-shape characteristics in the J–V curve of the resultant inverted perovskite photovoltaic cells on the first day (see Table 1) due to the recued potential loss at grain boundaries.[53,54] The trend of the grain sizes also influences the formation of s-shape characteristic in the J–V curves on the 80th day (see Fig. 2(b)), which means that the larger grains (less grain boundaries) result in less MA^+-PCBM-MA^+ cations, thereby reducing the formation of a $HPbI_3$ barrier at the PCBM/$MAPbI_3$ interface. Fig. 6(a) presents the main X-ray diffraction patterns of the $MAPbI_3$/P3CT-Na/ITO/glass samples fabricated with different drying times. The asymmetric curve indicates that the (110)-oriented peak and (002)-oriented peak overlapped.[55] To separate the diffraction

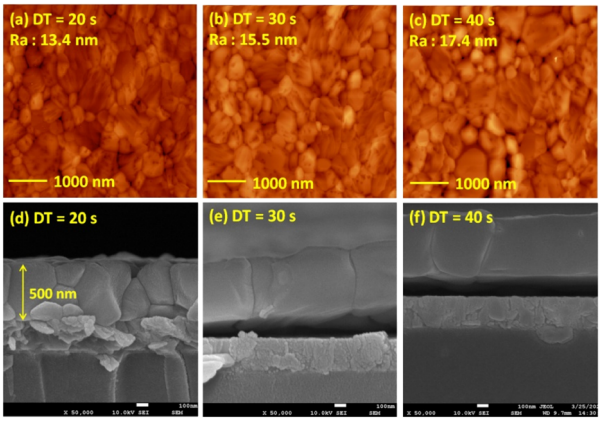

Fig. 5 Atomic-force microscopy (AFM) images and scanning electron microscopy (SEM) images of $MAPbI_3$/P3CT-Na/ITO/glass samples fabricated with different drying times (DTs). (a) AFM, DT = 20 s; (b) AFM, DT = 30 s; (c) AFM, DT = 40 s; (d) SEM, DT = 20 s; (e) SEM, DT = 30 s; (f) SEM, DT = 40 s.

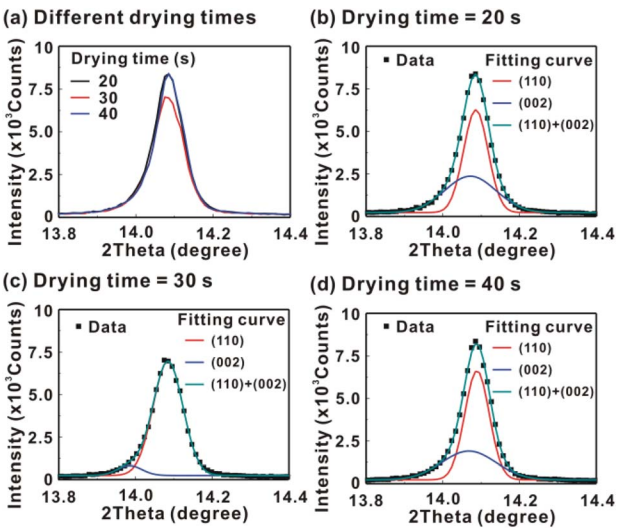

Fig. 6 (a) Main X-ray diffraction patterns of the $MAPbI_3$/P3CT-Na/ITO/glass samples fabricated with different drying times (DTs). (b) Fitting curves, DT = 20 s; (c) fitting curves, DT = 30 s; (d) fitting curves, DT = 40 s.

Table 2 Key features in the main XRD patterns, PL spectra and absorbance spectra of the $MAPbI_3$/P3CT-Na/ITO/glass sample. $MAPbI_3$ films are prepared with different drying times

Drying time	XRD peak intensity (counts)	2θ of the 002-peak (degree)	2θ of the 110-peak (degree)	Ratio of $I_{(110)}/I_{(002)}$	PL peak intensity (counts)	Slope of the absorbance curve (1/nm)
20 s	8141	14.072	14.086	1.36	48	−0.0097
30 s	6809	13.985	14.085	14.58	67	−0.0105
40 s	8141	14.070	14.090	1.72	38	−0.0088

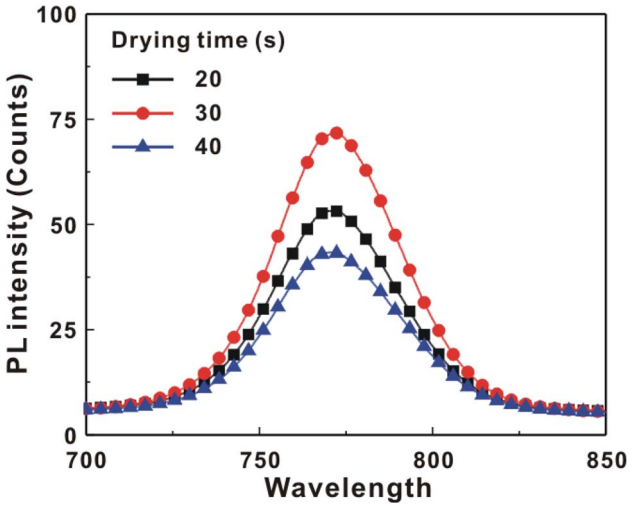

Fig. 7 Top-excited photoluminescence spectra of the $MAPbI_3$/P3CT-Na/ITO/glass samples fabricated with different drying times.

features of the two peaks, the asymmetric peaks are fitted with a two-Gaussian function. The fitting results are plotted in Fig. 6(b)–(d). The peak intensity values, the diffraction angles of peaks and the intensity ratio between the two peaks are listed in Table 2. The trend of the peak intensity values is inversely proportional to the trend of the (002)-peak position values, which is related to the lattice distortion of the $MAPbI_3$ crystalline thin films. As shown in Fig. 6(c), the diffraction angle of the (002) peak is shorter than the others, which means that the crystal plane distance along the (002) direction is longer than the others when the drying time is 30 s. In a (110)-oriented $MAPbI_3$ thin film, the (002) crystal plane is parallel to the intergrain surface. In other words, the longer crystal plane distance along the (002) direction can be explained due to the tensile stress from the interfacial contact and the formation of merged grains. Besides, the intensity ratio of the (110)-peak and (002)-peak (I_{110}/I_{002}) is the highest value (14.58) when the drying time is 30 s. In other words, the crystal orientation of the merged $MAPbI_3$ grains is also related to the surface properties of the P3CT-Na/ITO/glass substrate, thereby forming the (110) preferred $MAPbI_3$ crystalline thin film.[56] Fig. 7 presents the top-excited PL spectra of the $MAPbI_3$/P3CT-Na/ITO/glass samples fabricated with different drying times. The trend of the PL

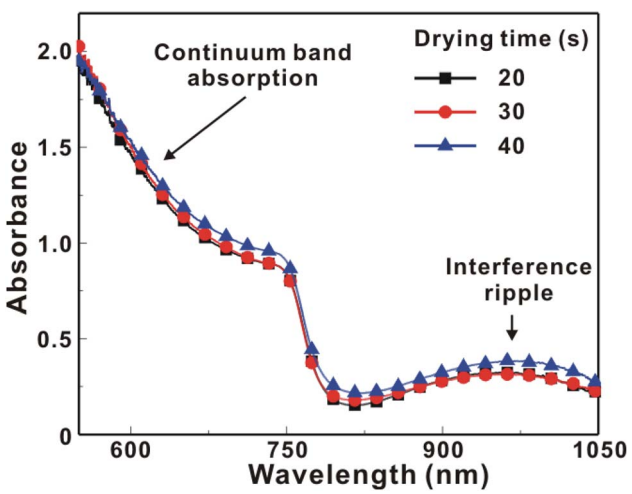

Fig. 8 Absorbance spectra of the $MAPbI_3$/P3CT-Na/ITO/glass samples fabricated with different drying times.

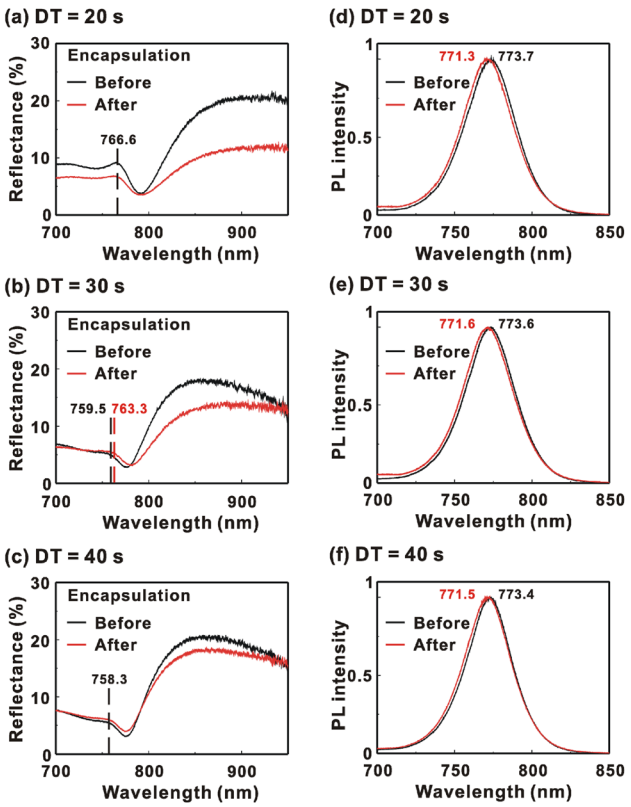

Fig. 9 Reflectance and photoluminescence (PL) spectra of the $MAPbI_3$/P3CT-Na/ITO/glass samples before and after encapsulation. $MAPbI_3$ films are fabricated with different drying times (DTs). (a) Reflectance, DT = 20 s; (b) reflectance, DT = 30 s; (c) reflectance, DT = 40 s; (d) PL, DT = 20 s; (e) PL, DT = 30 s; (f) PL, DT = 40 s.

Table 3 Reflectance peak wavelength and PL peak wavelength of the $MAPbI_3$/P3CT-Na/ITO/glass samples before encapsulation, after encapsulation and after 10 days. $MAPbI_3$ films are fabricated with different drying times

Encapsulation	Drying time	Reflectance peak wavelength, λ_R (nm)	PL peak wavelength, λ_{PL} (nm)	$\Delta\lambda = \lambda_{PL} - \lambda_R$ (nm)
Before	20 s	766.6	773.7	7.1
Before	30 s	759.5	773.6	14.1
Before	40 s	758.3	773.4	15.1
After	20 s	766.6	771.3	4.7
After	30 s	763.3	771.6	8.3
After	40 s	758.3	771.5	13.2

intensities is proportional to the trend of the I_{110}/I_{002} ratio values (see Table 2). When the drying time is 30 s, the PL intensity from the top region of the $MAPbI_3$ crystalline thin film corresponds to the highest value. When the drying time is reduced to 20 s, the relatively lower PL intensity can be explained as due to the higher defect density at the inter-gain boundaries of the $MAPbI_3$ crystalline thin film. When the drying time is extended to 40 s, the relatively lower PL intensity can be explained as due to the higher surface defect density of the rough $MAPbI_3$ crystalline thin film. Fig. 8 presents the absorbance spectra of the $MAPbI_3$/P3CT-Na/ITO/glass samples fabricated with different drying times. In the near-infrared wavelength range from 800 nm to 1050 nm, the formation of ripples is due to the thin-film interference between interfaces. The larger amplitude of the interference ripple indicates the weaker light scattering from the surface due to the lower roughness of the $MAPbI_3$ thin films.[57,58] The trend of the ripple amplitudes is inversely proportional to the trend of the Ra values (see Fig. 5). Besides, the higher absorbance is due to the larger Ra when the drying time is 40 s. In general, the slope of the absorbance curve in the continuum absorption band is inversely proportional to the exciton binding energy of the $MAPbI_3$ crystalline thin film.[59] It is noted that the trend of the exciton binding energies is inversely proportional to the trends of the J_{SC} values and FF values (see Table 1). In other words, the higher PCE of the inverted perovskite photovoltaic cells is also related to the lower exciton binding energy of the $MAPbI_3$ crystalline thin film due to the formation of merged and soft perovskite grains.

Fig. 9 presents the reflectance spectra and bottom-excited PL spectra of the $MAPbI_3$/P3CT-Na/ITO/glass samples before and after the encapsulation process. The $MAPbI_3$ crystalline thin films are fabricated with different drying times. The reflectance peak is related to the exciton transition of the $MAPbI_3$ crystalline thin film. According to the material dispersion relation, a longer exciton transition wavelength results in a longer reflectance peak wavelength due to the higher refractive index.[60] Therefore, the difference between the reflectance peak wavelength and the PL peak wavelength ($\Delta\lambda = \lambda_{PL} - \lambda_R$) is proportional to the Stokes shift (exciton binding energy). The reflectance peak wavelengths, PL peak wavelengths and $\Delta\lambda$ values of the $MAPbI_3$/P3CT-Na/ITO/glass samples are listed in Table 3. Before encapsulation, the trend of the $\Delta\lambda$ (exciton binding energy) values is proportional to the trend of the grain sizes (see Fig. 5(d)–(f)), which means that the formation of merged and soft grains results in lattice distortion, thereby increasing the $\Delta\lambda$ (exciton binding energy) in the bottom region of the $MAPbI_3$ crystalline thin film.[61] In other words, the extended drying time results in a distorted lattice in the bottom region of the $MAPbI_3$ crystalline thin film, thereby decreasing the atomic contact strength at the $MAPbI_3$/P3CT-Na interface (see Fig. 5(d) and (e)). In the aspect of the device performance of un-encapsulated photovoltaic cells on the first day, the average V_{OC} value increases from 1.010 V to 1.017 V with the increase in the drying time from 20 s to 40 s, which can be explained due to the increased grain size (decreased potential loss). However, the average J_{SC} (FF) value has the highest value when the drying time is 30 s, which is due to the better contact quality at the $MAPbI_3$/P3TC-Na interface and the lower exciton binding energy of the $MAPbI_3$ thin film.

After encapsulation, the decreased $\Delta\lambda$ values are 2.4, 5.8 and 1.9 nm when the drying times are 20, 30 and 40 s, respectively. It is noted that the trend of the decreased $\Delta\lambda$ (exciton binding energy) values is proportional to the trend of the increased V_{OC} values (see Table 1) after encapsulation. The decreased $\Delta\lambda$ (exciton binding energy) in the bottom region of the $MAPbI_3$ crystalline thin film can be explained as due to the formation of shallow defects after the encapsulation process, which increases the effective Fermi level for electrons of the soft $MAPbI_3$ crystalline thin film, thereby resulting in the higher V_{OC} of the inverted perovskite photovoltaic cells.

Conclusions

In summary, the open-circuit voltage of the inverted perovskite crystalline photovoltaic cells can be largely increased from 1.010 V to 1.156 V *via* the formation of merged and soft $CH_3NH_3PbI_3$ ($MAPbI_3$) grains and the reduced exciton binding energy (increased carrier density), which are confirmed by analyzing the surface morphologies, cross-sectional images, crystal structures and excitonic properties of the $MAPbI_3$/P3CT-Na/ITO/glass samples with and without encapsulation. It is noted that the photovoltaic cells maintain the average power conversion efficiency to be higher than 17.5% within 80 days when the $MAPbI_3$ thin film is fabricated with an optimized drying time of 30 s.

Conflicts of interest

There are no conflicts to declare.

Acknowledgements

Financial support was provided by the Ministry of Science and Technology (Taiwan) under Grants MOST 110-2112-M-033-008-MY3 and MOST 111-2112-M-033-008.

References

1 J. Y. Kim, J.-W. Lee, H. S. Jung, H. Shin and N.-G. Park, High-efficiency perovskite solar cells, *Chem. Rev.*, 2020, **120**, 7867–7918.
2 J. Zhang, W. Zhang, H.-M. Cheng and S. P. P. Silva, Critical review of recent progress of flexible perovskite solar cells, Mater, *Today*, 2020, **39**, 66–88.
3 M. Jost, L. Kegelmann, L. Korte and S. Albrecht, Monolithic perovskite tandem solar cells: A review of the present status and advanced characterization methods toward 30% efficiency, *Adv. Energy Mater.*, 2020, **10**, 1904102.
4 Y. Shen, M.-N. Li, Y. Li, F.-M. Xie, H.-Y. Wu, G.-H. Zhang, L. Chen, S.-T. Lee and J.-X. Tang, Rational interface engineering for efficient flexible perovskite light-emitting diodes, *ACS Nano*, 2020, **14**, 6107–6116.
5 X.-K. Liu, W. Su, S. Bai, Y. Jin, J. Wang, R. H. Friend and F. Gao, Metal halide perovskites for light-emitting diodes, *Nat. Mater.*, 2021, **20**, 10–21.
6 C.-C. Lee, J. Iskandar, A. K. Akbar, H.-M. Cheng and S.-W. Liu, Controllable crystallization based on the aromatic ammonium additive for efficiently near-infrared perovskite light-emitting diodes, *Org. Electron.*, 2021, **99**, 106327.
7 C. Bao, J. Yang, S. Bai, W. Xu, Z. Yan, Q. Xu, J. Liu, W. Zhang and F. Gao, High performance and stable all-inorganic metal halide perovskite-based photodetectors for optical communication applications, *Adv. Mater.*, 2018, **30**, 1803422.
8 H. Jing, R. Peng, R.-M. Ma, J. He, Y. Zhou, Z. Yang, C.-Y. Li, Y. Liu, X. Guo, Y. Zhu, D. Wang, J. Su, C. Sun, W. Bao and M. Wang, Flexible ultrathin single-crystalline perovskite photodetector, *Nano Lett.*, 2020, **20**, 7144–7151.
9 Z. Lan, L. Cai, D. Lu and F. Zhu, Narrowband near-infrared perovskite/polymer hybrid photodetectors, *ACS Appl. Mater. Interfaces*, 2021, **13**, 981–988.
10 C. Gu and J.-S. Lee, Flexible hybrid organic-inorganic perovskite memory, *ACS Nano*, 2016, **10**, 5413–5418.
11 Z. Xu, Z. Liu, Y. Huang, G. Zheng, Q. Chen and H. Zhou, To probe the performance of perovskite memory devices: defects property and hysteresis, *J. Mater. Chem. C*, 2017, **5**, 5810–5817.
12 X. Wu, H. Yu and J. Cao, Unraveling the origin of resistive switching behavior in organolead halide perovskite based memory devices, *AIP Adv.*, 2020, **10**, 085202.
13 H. Peng, J. Guo, G. Chen and W. Qin, Self-powered perovskite $CH_3NH_3PbBr_3$ field effect transistor with fast response and high sensitivity in sensing, *Mater. Today*, 2021, **12**, 100185.
14 B. Jeong, L. Veith, T. J. A. M. Smolders, M. J. Wolf and K. Asadi, Room-temperature halide perovskite field-effect transistors by ion transport mitigation, *Adv. Mater.*, 2021, **33**, 2100486.
15 H. Zhu, A. Liu, K. I. Shim, H. Jung, T. Zou, Y. Reo, H. Kim, J. W. Han, Y. Chen, H. Y. Chu, J. H. Lim, H.-J. Kim, S. Bai and Y.-Y. Noh, High-performance hysteresis-free perovskite transistors through anion engineering, *Nat. Commun.*, 2022, **13**, 1741.
16 W.-J. Yin, T. Shi and Y. Yan, Unique properties of halide perovskites as possible origins of the superior solar cell performance, *Adv. Mater.*, 2014, **26**, 4653–4658.
17 L. M. Herz, Charge-carrier mobilities in metal halide perovskites: Fundamental mechanisms and limits, *ACS Energy Lett.*, 2017, **2**, 1539–1548.
18 L. Chouhan, S. Ghimire, C. Subrahmanyam, T. Miyasaka and Y. Biju, Synthesis, optoelectronic properties and applications of halide perovskite, *Chem. Soc. Rev.*, 2020, **49**, 2869–2885.
19 S. H. Chang, K.-F. Lin, C.-H. Chiang, S.-H. Chen and C.-G. Wu, Plasmonic structure enhanced exciton generation at the interface between the perovskite absorber and copper nanoparticles, *Sci. World J.*, 2014, **2014**, 128414.
20 F. Ruf, M. F. Ayguler, N. Ciesbrecht, B. Rendenbach, A. Magin, P. Docampo, H. Kalt and M. Hetterich, Temperature-dependent studies of exciton binding energy and phase-transition suppression in $(Cs,FA,MA)Pb(I,Br)_3$ perovskites, *APL Mater.*, 2019, **7**, 031113.
21 Y. Liu, Z. Yang and S. F. Liu, Recent progress in single-crystalline perovskite research including crystal preparation, property evaluation, and applications, *Adv. Sci.*, 2018, **5**, 1700471.
22 J. Jeong, M. Kim, J. Seo, H. Lu, P. Ahlawat, A. Mishra, Y. Yang, H. A. Hope, F. T. Eickemeyer, M. Kim, Y. J. Yoon, I. W. Choi, B. P. Darwich, S. J. Choi, Y. Jo, Y. H. Lee, B. Walker, S. M. Zakeeruddin, L. Emsley, U. Rothlisberger, A. Hagfeldt, D. S. Kim, M. Gratzel and J.-Y. Kim, Pesudo-halide anion engineering for α-$FAPbI_3$ perovskite solar cells, *Nature*, 2021, **592**, 381–385.
23 Z. Li, B. Li, X. Wu, S. A. Sheppard, S. Zhang, D. Gao, N. J. Long and Z. Zhu, Organometallic-functionalized interfaces for highly efficient inverted perovskite solar cells, *Science*, 2022, **376**, 416–420.
24 H. Li, G. Wu, W. Li, Y. Zhang, Z. Liu, D. Wang and S. F. Liu, Additive engineering to grow micron-sized grains for stable high efficiency perovskite solar cells, *Adv. Sci.*, 2109, **6**, 1901241.
25 G. Lu, W. Zhu, F. He, D. Chen, C. Zhang and Y. Hao, Enhanced sensitivity of grain sizes to precursor stoichiometry enables high-quality $CH_3NH_3PbI_3$ films for efficient perovskite solar cells, *Mater. Lett.*, 2019, **250**, 88–91.
26 M. Nukunudompanich, G. Budiutama, K. Suzuki, K. Hasegawa and M. Ihara, Dominant effect of the grain size of the $MAPbI_3$ perovskite controlled by the surface roughness of TiO_2 on the perovskite of perovskite solar cells, *CrystEngComm*, 2022, **22**, 2718–2727.
27 S. H. Chang, K.-F. Lin, H.-M. Cheng, C.-C. Chen, W.-T. Wu, S.-H. Chen and C.-G. Wu, Influence of organic cations on

high-performance $CH_3NH_3PbI_3$ based photovoltaics, *Sol. Energy Mater. Sol. Cells*, 2016, **145**, 375–381.

28 C.-C. Chen, S. H. Chang, L.-C. Chen, H.-M. Cheng, Z.-L. Tseng and C.-G. Wu, Manipulating multicrystalline grain size in $CH_3NH_3PbI_3$ thin films for application in photovoltaics, *Sol. Energy*, 2016, **139**, 518–523.

29 S. H. Chang, W.-C. Huang, C.-C. Chen, S.-H. Chen and C.-G. Wu, Effects of anti-solvent (iodobenzene) volume on the formation of $CH_3NH_3PbI_3$ thin films and their application in photovoltaic cells, *Appl. Surf. Sci.*, 2018, **445**, 24–29.

30 F. Giordano, A. Abate, J. P. C. Banea, H. Saliba, T. Matsui, S. H. Im, S. M. Zakeeruddin, M. K. Nzeeruddin, A. Hagfeldt and M. Gratzel, Enhanced electronic properties in mesoporous TiO_2 *via* lithium doping for high-efficiency perovskite solar cells, *Nat. Commun.*, 2016, **7**, 10379.

31 S. H. Chang, W.-N. Chen, C.-C. Chen, S.-C. Yeh, H.-M. Cheng, Z.-L. Tseng, L.-C. Chen, K. Y. Chiu, W.-T. Wu, C.-T. Chen, S.-H. Chen and C.-G. Wu, Manipulating the molecular structure of PEDOT chains through controlling the viscosity of PEDOT:PSS solution to improve the photovoltaic performance of $CH_3NH_3PbI_3$ solar cells, *Sol. Energy Mater. Sol. Cells*, 2017, **161**, 7–13.

32 S. Shao and M. A. Loi, The role of the interfaces in perovskite solar cells, *Adv. Mater. Interfaces*, 2020, **7**, 1901469.

33 S. Li, B. He, J. Xu, H. Liu, J. Jiang, J. Zhu, Z. Kan, L. Zhu and F. Wu, Highly efficient inverted perovskite solar cells incorporating P3CT-Rb as a hole transport layer to achieve a large open circuit voltage of 1.144 V, *Nanoscale*, 2020, **12**, 3686–3691.

34 S. Li, H. Lu, Z. Kan, L. Zhu and F. Wu, Engineering of P3CT-Na through diprophylline treatment to realilze efficient stable inverted perovskite solar cells, *Chem. Eng. J.*, 2021, **419**, 129581.

35 J. Xu, J. Dai, H. Dong, P. Li, J. Chen, X. Zhu, Z. Wang, B. Jiao, X. Hou, J. Li and Z. Xu, Surface-tension release in PTAA-based inverted perovskite solar cells, *Org. Electron.*, 2022, **100**, 106378.

36 C.-Y. Li, A. Chandel, J.-R. Wu, D. Thakur, S.-E. Chiang, K.-R. Cheng, S.-H. Chen, J.-L. Shen and S. H. Chang, Highly efficient and stable P3CT-Na based $MAPbI_3$ solar cells with a Sn-rich ITO anode, *Sol. Energy Mater. Sol. Cells*, 2021, **231**, 111305.

37 S.-E. Chang, Q.-B. Ke, A. Chandel, H.-M. Cheng, Y.-S. Yen, J.-L. Shen and S. H. Chang, 19% efficient P3CT-Na based $MAPbI_3$ solar cells with a simple double-filtering process, *Polymers*, 2021, **13**, 886.

38 Q. Zhou, J. Qu, Y. Wang, M. Yu, J. Liu and X. Zhang, Multifunctional chemical bridge and defect passivation for highly efficient inverted perovskite solar cells, *ACS Energy Lett.*, 2021, **6**, 1596–1606.

39 Q. B. Ke, J.-R. Wu, C.-C. Lin and S. H. Chang, Understanding the PEDOT:PSS, PTAA and P3CT-X hole-transport-layer-based inverted perovskite solar cells, *Polymers*, 2022, **14**, 823.

40 M. Fang, L. Tao, W. Wu, Q. Wei, Y. Xia, P. Li, X. Ran, Q. Zhong, G. Xing, L. Song, P. Muller-Buschbaum, H. Zhang and Y. Chen, Residual solvent extraction *via* chemical displacement for efficient and stable perovskite solar cells, *J. Energy Chem.*, 2021, **61**, 8–14.

41 Y. Zhou, A. Najar, J. Zhang, J. Feng, Y. Cao, Z. Li, X. Zhu, D. Yang and S. F. Liu, Effect of solvent residue in the thin-film fabrication on perovskite solar cell performance, *ACS Appl. Mater. Interfaces*, 2022, **14**, 28729–28737.

42 J. Li, Y. Han, W. Jiang, P. Huang, R. Cai, M. Wang and J. Bian, Key role of residual lead iodide in two-step processed perovskite layer for high performance perovskite solar cells, *Appl. Phys. Lett.*, 2023, **122**, 013901.

43 T. Thakur, Q. B. Ke, S.-E. Chiang, T.-H. Tseng, K.-B. Cai, C.-T. Yuan, J.-S. Wang and S. H. Chang, Stable and efficient soft perovskite crystalline film based solar cells prepared with a facile encapsulation method, *Nanoscale*, 2022, **14**, 17625–17632.

44 Q. B. Ke, J.-R. Wu, S.-E. Chiang, C.-C. Cheng, Y.-W. Su, I.-J. Hsu, J.-M. Yeh and S. H. Chang, Improved performance of PCBM/$MAPbI_3$ heterojunction photovoltaic cells with the treatment of a saturated BCP/IPA solution, *Sol. Energy Mater. Sol. Cells*, 2022, **242**, 111782.

45 S.-E. Chiang, A. Chandel, D. Thakur, Y.-T. Chen, P.-C. Lin, J.-R. Wu, K.-B. Cai, S. Kassou, J.-M. Yeh, C.-T. Yuan, J.-L. Shen and S. H. Chang, On the role of solution-processed bathocuproine in high-efficiency inverted perovskite solar cells, *Sol. Energy*, 2021, **218**, 142–149.

46 S. H. Chang, P.-C. Tseng, S.-E. Chiang, J.-R. Wu, Y.-T. Chen, C.-J. Chen, C.-T. Yuan and S.-H. Chen, Structural, optical and excitonic properties of $MA_xCs_{1-x}Pb(I_xBr_{1-x})_3$ alloy thin films and their application in solar cells, *Sol. Energy Mater. Sol. Cells*, 2020, **210**, 110478.

47 A. Chandel, Q. B. Ke, D. Thakur, S.-E. Chiang, J.-R. Wu, K.-B. Cai, C.-T. Yuan and S. H. Chang, Regioregularity effects of p-type P3CT-Na polymers on inverted perovskite photovoltaic cells, *Org. Electron.*, 2022, **102**, 106449.

48 S.-E. Chiang, J.-R. Wu, H.-M. Cheng, C.-L. Hsu, J.-L. Shen, C.-T. Yuan and S. H. Chang, Origins of the s-shape characteristic in J-V curve of inverted-type perovskite solar cells, *Nanotechnology*, 2020, **31**, 115403.

49 Y. He, W. Wang and L. Qi, $HPbI_3$ as a bifunctional additive for morphology control and grain boundary passivation toward efficient planar perovskite solar cells, *ACS Appl. Mater. Interfaces*, 2018, **10**, 38985–38993.

50 D. Thakur, S.-E. Chiang, M.-H. Yang, J.-S. Wang and S. H. Chang, Self-stability of un-encapsulated polycrystalline MAPbI3 solar cells *via* the formation of chemical bonds between C_{60} molecules and MA cations, *Sol. Energy Mater. Sol. Cells*, 2022, **235**, 111454.

51 S. Parveen and P. K. Giri, Emerging doping strategies in two-dimensional hybrid perovskite semiconductors for cutting edge optoelectronics applications, *Nanoscale Adv.*, 2022, **4**, 995–1025.

52 M. Lai, A. Obliger, D. Lu, C. S. Kley, C. G. Bischak, Q. Kong, T. Lei, L. Dou, N. S. Ginsberg, D. T. Limmer and P. Yang, Intrinsic anion diffusivity in lead halide perovskites is facilitated by a soft lattice, *Proc. Natl. Acad. Sci. U. S. A.*, 2018, **115**, 11929–11934.

53 J.-W. Lee, S.-H. Bae, N. De Marco, Y.-T. Hsieh, Z. Dai and Y. Yang, The role of grain boundaries in perovskite solar cells, *Mater. Today Energy*, 2018, **7**, 149–160.

54 D. Thakur, J.-R. Wu, A. Chandel, K.-J. Cheng, S.-E. Chiang, K.-B. Cai, S.-H. Chen, C.-C. Yang, Y.-L. Zhong, C.-T. Yuan, J.-L. Shen and S. H. Chang, Structural, optical and excitonic properties of urea grading doped CH3NH3PbI3 thin films and their application in inverted-type perovskite solar cells, *J. Alloys Compd.*, 2021, **858**, 157660.

55 C.-Y. Li, Y.-S. Liao, D. Thakur, A. Chandel, S.-E. Chiang, J.-R. Wu, P.-H. Lee, C.-L. Tsai, C.-C. Yang, Y.-L. Zhong, J.-L. Shen and S. H. Chang, Anti-solvent mixture-mediated reduction of photocurrent hysteresis in high-impurity perovskite precursor based $MAPbI_3$ solar cells, *Sol. Energy*, 2021, **214**, 86–92.

56 S. Kassou, J.-R. Wu, D. Thakur, A. Chandel, S.-E. Chiang, K.-J. Cheng, S.-H. Chen, J.-L. Shen and S. H. Chang, Efficiency improvement of P3CT-Na based $MAPbI_3$ solar cells with a simple wetting process, *Nanotechnology*, 2021, **32**, 345402.

57 S. H. Chang, W.-C. Huang, C.-C. Chen, S.-H. Chen and C.-G. Wu, Effects of anti-solvent (iodobenzene) volume on the formation of CH3NH3PbI3 thin films and their application in photovoltaic cells, *Appl. Surf. Sci.*, 2018, **445**, 24–29.

58 S. H. Chang, S.-D. Wong, H.-Y. Huang, C.-T. Yuan, J.-R. Wu, S.-E. Chiang, Z.-L. Tseng and S.-H. Chen, Effects of the washing-enhanced nucleation process on the material properties and performance of perovskite solar cells, *J. Alloys Compd.*, 2019, **808**, 151723.

59 N. Sestu, M. Cadelano, V. Sarritzu, F. Chen, D. Marongiu, R. Piras, M. Mainas, F. Quochi, M. Saba, A. Mura and G. Bongiovanni, Absorption F-sum rule for the exciton binding energy in methylammonium lead halide perovskites, *J. Phys. Chem. Lett.*, 2015, **6**, 4566–4572.

60 Y. Jiang, A. M. Soufiani, A. Gentle, F. Huang, A. H. Baillie and M. A. Green, Temperature dependent optical properties of $CH_3NH_3PbI_3$ perovskite by spectroscopic ellipsometry, *Appl. Phys. Lett.*, 2016, **108**, 061905.

61 S. Feldmann, M. K. Gangishetty, I. Bravic, T. Neumann, B. Peng, T. Winkler, R. H. Friend, B. Monserrat, D. N. Congreve and F. Deschler, Charge carrier localization in doped perovskite nanocrystals enhances radiative recombination, *J. Am. Chem. Soc.*, 2021, **143**, 8647–8653.